Atmos. Chem. Phys. Discuss., 12, 559–587, 2012
www.atmos-chem-phys-discuss.net/12/559/2012/
doi:10.5194/acpd-12-559-2012

Atmospheric Chemistry and Physics Discussions

CO at 40–80 km above Kiruna observed by the ground-based microwave radiometer KIMRA and simulated by the whole atmosphere community climate model

C. G. Hoffmann[1], D. E. Kinnison[2], R. R. Garcia[2], M. Palm[1], J. Notholt[1], U. Raffalski[3], and G. Hochschild[4]

[1]Institute of Environmental Physics, University Bremen, Germany
[2]National Center for Atmospheric Research, Boulder, Colorado, USA
[3]Swedish Institute of Space Physics, Kiruna, Sweden
[4]Institute for Meteorology and Climate Research, Karlsruhe Institute of Technology, Germany

Received: 22 November 2011 – Accepted: 16 December 2011 – Published: 6 January 2012

Correspondence to: C. G. Hoffmann (christoph.hoffmann@iup.physik.uni-bremen.de)

Published by Copernicus Publications on behalf of the European Geosciences Union.

Abstract

This study compares CO in the Arctic stratosphere and mesosphere measured by ground-based microwave radiometry with simulations made with the Whole Atmosphere Community Climate Model driven with specified dynamical fields (SD-WACCM4) for the Arctic winters 2008/2009 and 2009/2010. CO is a tracer for polar winter middle atmosphere dynamics, hence the representation of polar dynamics in the model is examined indirectly. Measurements were taken with the Kiruna Microwave Radiometer (KIMRA). The instrument, which is located in Kiruna, Northern Sweden (67.8° N, 20.4° E), provides CO profiles between 40 and 80 km altitude.

The present comparison, which is one of the first between SD-WACCM4 and measurements, is performed on the smallest space and time scales currently simulated by the model; the global model is evaluated daily at the particular model grid-point closest to Kiruna. As a guide to what can generally be expected from such a comparison, the same analysis is repeated for observations of CO from the Microwave Limb Sounder (MLS), a microwave radiometer onboard NASA's Aura satellite, which has global coverage. First, time-mean profiles of CO are compared, revealing that the profile shape of KIMRA deviates from SD-WACCM4 and MLS, especially in the upper mesosphere. SD-WACCM4 and MLS are mostly consistent throughout the range of altitude considered; however, SD-WACCM4 shows slightly lower values above 60 km and this discrepancy increases with altitude. Second, the time evolution is compared for the complete time series, as well as for the slowly and rapidly evolving parts alone. Overall, the agreement among the datasets is very good and the model is almost as consistent with the measurements as the measurements are with each other. Mutual correlation coefficients of the slowly varying part of the CO time series are $\geq$0.9 over a wide altitude range. This demonstrates that the polar winter middle atmosphere dynamics is very well represented in SD-WACCM4 and that the relaxation to analyzed meteorological fields below 50 km constrains the behavior of the simulation sufficiently, even at higher altitudes, such that the simulation above 50 km is close to the measurements.

ACPD

12, 559–587, 2012

However, above 50 km, the model-measurement correlation for the rapidly varying part of the CO time series is lower (0.3) than the measurement-measurement correlation (0.6). This is attributed to the fact that the gravity wave parametrization in WACCM is based on a generic gravity wave spectrum and cannot be expected to capture the instantaneous behavior of the actual gravity wave field present in the atmosphere.

1 Introduction

The dynamics of the polar middle atmosphere exhibits strong variability on different time scales, which is of importance for other atmospheric features, particularly for the ozone layer (e.g., Shepherd, 2007). Seasonal changes are dominated by the reversal of the mean circulation from the winter regime – with a strong westerly zonal wind and a mean meridional circulation toward the winter pole, with descent in high latitudes – to the summer regime with roughly opposite wind directions. The strongest feature of intra-seasonal variability in winter are major sudden stratospheric warmings (SSW), during which the polar vortex may vanish completely and the circulation may switch to summer-like conditions for a limited time period before the vortex is reestablished. Generally, variability on small temporal and spatial scales is introduced by the variable wave activity in the middle atmosphere (e.g., Fritts et al., 2006). This is particularly true for the Northern Hemisphere, where wave activity is stronger. Furthermore, the overall evolution of the polar winter exhibits a strong interannual variability. In the Arctic, two unusual events occurred is the past few years: in spring 2009 the strongest SSW on record developed (Manney et al., 2009), although a comparatively undisturbed winter might have been expected considering statistical relationships related to, e.g., the Quasi-Biennial Oscillation and the sunspot cycle (Labitzke and Kunze, 2009). In contrast, the polar vortex in the winter 2010/2011 was exceptionally strong and persistent, and led to the strongest Arctic spring ozone depletion on record, with ozone loss approaching that observed in Antarctic spring (Manney et al., 2011). This shows that the understanding of the Arctic middle atmosphere dynamics is still incomplete and has to be improved by further observations and their simulation by models.

ACPD
12, 559–587, 2012

A good tracer for dynamics in the polar winter is CO, since its photochemical lifetime in these conditions is comparable to transport timescales (Solomon et al., 1985; Minschwaner et al., 2010). Furthermore, the CO vmr profile shows a steep increase from the stratosphere to the lower thermosphere, which makes the tracer CO sensitive to vertical motions. Additionally, CO also exhibits during winter strong horizontal gradients at the polar vortex boundary, such that it is also sensitive to horizontal transport. The quantitative interpretation of CO data is therefore complex. However, modeled CO can be compared directly with observations, which strictly examines the overall representation of all processes influencing CO in the model, not just the model dynamics.

The time evolution of CO simulated with the Whole Atmosphere Community Climate Model (WACCM), the basis of the model which is examined in this work, has already been compared to ground-based microwave measurements by Forkman et al. (2003) for a mid-latitude location. They find a generally good agreement of model and observations in the seasonal behavior, as well as a similar strength of the intra-seasonal variations. Their measurements show a higher interannual variability than WACCM, but unfortunately, the database is too small to be conclusive in this respect. Borsdorff and Sussmann (2009) generally support the findings of Forkman et al. (2003) using ground-based Fourier transform infrared spectroscopy (FTIR) measurements from different stations. However, these comparisons are limited by the fact that WACCM is a free-running model, so that model results and observations can only be compared in a statistical sense.

Recently, a new version of WACCM, SD-WACCM4 (or "specified dynamics" WACCM, version 4), has been developed. SD-WACCM4 is relaxed to analyzed meteorological data below a specified altitude, typically no greater than 50 km. The modeled time evolution is therefore constrained by the real world evolution, as represented in the meteorological analysis, and hence is directly comparable to measurements. The benefit of a comparison of SD-WACCM4 output against measurements is therefore twofold: First, the performance of SD-WACCM4 itself is examined, which is important for future studies, which are directly build upon this SD version. Second, a successful comparison

ACPD
12, 559–587, 2012

based on SD-WACCM4 also helps validate the overall quality of WACCM, since the free-running and SD versions of the model use essentially the same numerics.

In this work, we perform one of the first comparisons of SD-WACCM4 to measured data (Funke et al., 2011, as well as Marsh, 2011, have also carried out SD-WACCM4 comparisons). In particular, daily middle atmospheric CO vmr profiles for Arctic winter are compared against CO measured with the ground-based Kiruna Microwave Radiometer (KIMRA) in Kiruna, Northern Sweden (Hoffmann et al., 2011). We benefit thereby from the particular advantage of ground-based measurements, which provide a consistent time series for one particular location with a high temporal resolution. Thus, the representation of CO in SD-WACCM4 and, consequently, the representation of the dynamical variability described above, is examined on the smallest space and time scales currently simulated by the model; model output is taken from a single grid point, which is closest to Kiruna (instead of, e.g., in a zonal mean sense) and on each model day of the period analyzed. As a guide to what can be expected generally from a comparison of a single-point measurement to a spatially distributed dataset, we have also included in the analysis global CO measurements made by the Microwave Limb Sounder (MLS), onboard NASA's Aura satellite. The datasets used in our study are described in Sect. 2. In Sect. 3 mean CO profiles are compared, while the time evolution of CO is compared in Sect. 4. Our conclusions are presented in Sect. 5.

2 Data and model

2.1 Kiruna microwave radiometer (KIMRA)

The KIMRA dataset used in this work, KIMRA CO version 1.1, has been described and characterized in detail by Hoffmann et al. (2011). The KIMRA instrument is operated in Kiruna, Northern Sweden (67.8° N, 20.4° E, 425 m elevation) at the Swedish Institute of Space Physics (Institutet för Rymdfysik, IRF). At this location, the state of the middle atmosphere during winter is mainly influenced by conditions within the polar vortex.

ACPD
12, 559–587, 2012

However, mid-latitude air may be observed during several occasions in winter, since Kiruna is close to the Arctic circle and the vortex boundary occasionally passes over this location. The dataset of CO vmr profiles covers the winters 2008/2009 (December 2008 to April 2009) and 2009/2010 (September 2009 to April 2010). It contains 1500 profiles measured with 1 h integration time on average distributed over 300 days during the whole period.

The retrieval of each vmr profile, $\hat{\boldsymbol{x}}$, was performed using the optimal estimation technique (Rodgers, 2000), which requires as input an a priori profile of CO, $\boldsymbol{x}_a$, together with adjacent temperature and pressure profiles. The retrieval is performed on a pressure grid that corresponds to fixed altitudes with a spacing of 1 km between 0.5 and 130.5 km. This grid was selected to enhance the numerical stability of the retrieval calculations but represents neither the vertical resolution nor the reliable vertical range ("range of sensitivity") of the retrieved profiles. These characteristics are derived from the "averaging kernel" (AVK) functions that are also a part of the retrieval output and may vary slightly among the profiles. One AVK function measures the sensitivity of the retrieved value, $\hat{x}^i$, at altitude z^i to perturbations of the true state in any single altitude considered in the retrieval. For the numerical processing, all the AVK functions are stored in a matrix, **A**, with each row representing the AVK of the respective target altitude. The connection between the retrieved profile, $\hat{\boldsymbol{x}}$, with the real state of the atmosphere, $\boldsymbol{x}_I$, is given by the following equation (Rodgers, 2000), demonstrating that the retrieval result is generally influenced by both the atmospheric state, as well as the retrieval and instrument characteristics.

$$\hat{\boldsymbol{x}}_I = \boldsymbol{x}_a + \mathbf{A}(\boldsymbol{x}_I - \boldsymbol{x}_a) \quad (1)$$

For a perfect measurement, **A** would be the unity matrix **I** (i.e., the a priori and the instrument characteristics would have no influence), but in reality **A** contains Gaussian-like peaked functions. A measure for the sensitivity at a certain altitude is the area under the respective AVK function, which should be close to one. The vertical resolution is indicated by the full width at half mean (FWHM) of the AVK function.

ACPD
12, 559–587, 2012

Hoffmann et al. (2011) carried out an analysis of the KIMRA CO AVKs; in this work we use their representation, $\mathbf{A}_{\mathrm{vmr}}$, as the AVK matrix $\mathbf{A}$. Under the assumption that altitudes with an AVK area greater than 0.8 have sufficient sensitivity, the KIMRA CO profiles are generally reliable between 40 and 80 km; however, the retrieval quality decreases already between 70 and 80 km. Figure 1 (left) shows the area of the AVKs in this region, demonstrating that the sensitivity usually deviates from one in the region that is considered to be reliable, which is a common behavior for these retrievals. The deviation of the sensitivity from one (Fig. 1, right) exhibits a shape with two minima (at about 52 and 72 km altitude) and three maxima (at approximately 40, 60, and 80 km altitude). These characteristics are of interest for interpreting the KIMRA data, as discussed in Sect. 4.

The KIMRA CO profiles provide vertical resolution of only 16 to 22 km, and the resolution becomes coarser with altitude (Hoffmann et al., 2011). This has to be considered in comparisons with datasets that have better vertical resolution. For this purpose, Eq. (1) is applied with $\boldsymbol{x}_{\mathrm{I}}$ set equal to the profile of the better-resolved dataset. This convolution with the KIMRA AVK matrix, $\mathbf{A}$, transforms the original profile $\boldsymbol{x}_{\mathrm{I}}$ according to the KIMRA instrument and retrieval characteristics. The result $\hat{\boldsymbol{x}}_{\mathrm{I}}$ is therefore the profile that would have been retrieved from a KIMRA measurement if $\boldsymbol{x}_{\mathrm{I}}$ had been the true state of the atmosphere at the time of the measurement. These convolved profiles $\hat{\boldsymbol{x}}_{\mathrm{I}}$ are therefore a representation of the independent CO datasets that are directly comparable to the KIMRA retrieval results. This means, in turn, that differences between different datasets can only be analyzed within the limits of the KIMRA sensitivity.

2.2 Microwave Limb Sounder

The Microwave Limb Sounder (MLS) is an instrument flying on the Aura satellite in a sun-synchronous polar orbit. It measures microwave emission of different species, including CO, in limb viewing geometry (Waters et al., 2006). The dataset provides by far the largest number of possible coincidences with KIMRA among the recent satellite datasets of CO in the middle atmosphere, so that comparatively tight collocation criteria

ACPD
12, 559–587, 2012

can be applied. Furthermore, the complete analyzed period of KIMRA measurements and the complete vertical range of sensitivity of KIMRA are covered, making the MLS dataset the ideal reference dataset for the present study.

For the comparison, the recent version 3.3 of the MLS CO product was used. The previous version 2.2 was validated by Pumphrey et al. (2007). The changes from version 2.2 to 3.3 are described in the version 3.3 quality document (Livesey et al., 2011). The KIMRA profiles were previously compared to the MLS profiles (version 3.3) and to two other recent satellite datasets of CO in Hoffmann et al. (2011).

2.3 Whole Atmosphere Community Climate Model

The Whole Atmosphere Community Climate Model, version 4 (WACCM4) is a comprehensive chemistry-climate model, which is fully interactive, such that the radiatively active gases affect heating and cooling rates and therefore dynamics. The model is based upon an earlier version, documented by Garcia et al. (2007), and updated with revisions to the gravity wave parameterization and the addition of a "turbulent mountain stress" parameterization to simulate the effect of unresolved topography (Richter et al., 2010). The model domain extends from the surface to the lower thermosphere (about 140 km geometric altitude). There are 66 levels in the vertical, with resolution of a little over 1 km in the troposphere and lower stratosphere, increasing to about 3.5 km in the lower thermosphere. The horizontal resolution is $1.9^{\circ} \times 2.5^{\circ}$ in latitude and longitude.

The chemical module of WACCM4 is based upon the 3-D chemical transport Model for Ozone and Related Chemical Tracers (MOZART), Version 3 (Kinnison et al., 2007). WACCM4 includes a detailed representation of the chemical and physical processes in the troposphere through the lower thermosphere. The species included within this mechanism are contained within the O_x, NO_x, HO_x, ClO_x, and BrO_x chemical families, along with CH_4 and its degradation products. In addition, fourteen primary non-methane hydrocarbons and related oxygenated organic compounds are included (Emmons et al., 2010). This mechanism contains 122 species, more than

ACPD
12, 559–587, 2012

220 gas-phase reactions, 71 photolytic processes, and 18 heterogeneous reactions on multiple aerosol types.

WACCM4 is typically used as a free-running climate model, coupled to an ocean model. Recently, a new version of the WACCM4 model has been developed that allows the model to be run with relaxation to externally specified meteorological fields (Lamarque et al., 2011). For the present study, the meteorological fields are taken from the Goddard Earth Observing System Model, Version 5 (GEOS-5) of NASA's Global Modeling and Assimilation Office (GMAO). The meteorological variables (i.e., temperature, zonal and meridional winds, and surface pressure) are used to constrain the model dynamics and to drive the physical parameterizations that control boundary layer exchanges, convective transport, and the hydrological cycle. The relaxation to GEOS-5 data is applied from the surface to 50 km altitude. This approach essentially turns WACCM4 into a chemical transport model and will be referred to as "specified-dynamics WACCM4" (SD-WACCM4). SD-WACCM4 output may be compared meaningfully to a specific set of observations even above the range of altitude where the model is constrained to GEOS-5 data because the constrained domain, below 50 km, has a strong influence on the behavior in the unconstrained domain, in the mesosphere and lower thermosphere. As shown by, e.g., Liu et al. (2010) and supported by the present study, the upper atmosphere is to a very great extent "driven" by the behavior of the lower atmosphere, such that, if the latter is constrained, the behavior of the former is also strongly conditioned by the constraint.

The SD-WACCM4 simulation used here constrains the model by replacing, at each time step, the model-predicted fields, $\mathbf{y}$, with a combination of these fields and the GEOS-5 data, $\mathbf{y}'$, according to:

$$\mathbf{y}(t) = 0.99\mathbf{y}(t) + 0.01\mathbf{y}'(t) \quad (2)$$

Given the model time step of 0.5 h, this corresponds to a relaxation of the model fields to the analysis with a time constant of approximately 2 days. As noted above, this relaxation scheme is used below 50 km. Above 60 km the model is free-running, as in WACCM4, with a linear transition region in between. With the effective relaxation

ACPD
12, 559–587, 2012

constant of 2 days, SD-WACCM4 simulates meteorological conditions very close to the original meteorological values. The SD-WACCM4 simulation employed here covers the period from 1 December 2004 through 1 January 2011. For these simulations the model was "spun up" from 1980 to the end of 2003 in fully interactive mode, i.e., without specified dynamics. On 1 January 2004 the model was switched to the SD-WACCM4 configuration with relaxation to GEOS-5 data according to Eq. (2).

A few words of explanation regarding the gravity wave parameterization used in WACCM are in order, as the characteristics of this parameterization are expected to affect the degree of agreement between the model and observations. Comprehensive models of the atmosphere that extend to very high altitude must take into account the effects of dissipating mesoscale gravity waves, since these play a major role in the momentum and constituent budgets of the atmosphere above about 50 km (e.g., Garcia and Solomon, 1985). Mesoscale gravity waves have typical horizontal wavelength of about 100 km, such that they cannot be resolved in global models such as WACCM. Instead, their effects are parameterized following the work of, e.g., Lindzen (1981). In practice, at model grid points in the troposphere, a "source" spectrum of gravity waves is launched and its propagation and dissipation are calculated as functions of altitude. The results of this calculation are then used to estimate the acceleration of the resolved winds, as well as mixing due to induced vertical diffusion (for details, see Garcia et al., 2007).

The source spectrum used in the gravity wave parameterization is based on observational estimates of the momentum flux due to vertically-propagating, mesoscale gravity waves. This spectrum is modified as it propagates through the stratosphere according to the winds in that region, which are relaxed to the GEOS-5 dataset as noted above. The modification of the upward-propagating gravity wave spectrum conditions the timing and intensity of wave breaking at higher altitudes, which drives the circulation in the mesosphere and lower thermosphere. In this sense, the large-scale circulation resolved by the model may be expected to correspond to the large-scale circulation of the upper atmosphere. However, the details of the actual gravity wave spectrum that

ACPD
12, 559–587, 2012

might be present in the atmosphere at any given time are not captured by the source spectrum specified in the parameterization, which is realistic only in a statistical, or climatological, sense. Therefore, the effects of the gravity wave parameterization on the model-resolved fields, are not expected to correspond to the detailed (small-scale, high-frequency) state of the real atmosphere at any given time. We discuss in Sect. 4.3 the role that parameterized gravity waves might play in the correlation between model results and observations.

2.4 Preprocessing

During preprocessing, subsets of the spatially distributed datasets are generated first. For SD-WACCM4, two different subsets are created. The first one, referred to as "SDWACCM", simply considers the closest grid-box (67.3° N, 20.0° E) to the measurement location and refers therefore mostly to the ground-based measurement approach. The second SD-WACCM4 subset, called "SDWACCM AREA", represents the satellite measurement approach; thus, the same collocation criteria as for MLS are applied: first, profiles have to be measured in a circle around Kiruna that has the radius R ($R = 200$ km) and second, they have to be measured on the same day.

These subsets of SD-WACCM4 and MLS are then interpolated vertically on the KIMRA retrieval grid and convolved with the KIMRA AVK using Eq. (1), so that the better-resolved profiles of SD-WACCM4 and MLS are smoothed and are directly comparable to the KIMRA measurements.

The temporal grid is unified by averaging the coincident profiles daily, so that the resulting time series contains one profile per day and dataset. However, the measured datasets may still have gaps due to missing measurements or the application of the collocation criteria.

ACPD
12, 559–587, 2012

3 Comparison of mean profiles

Mean profiles for all datasets, averaged over the complete analyzed period, were calculated to find possible systematic deviations. To do this, periods with data gaps in any of the preprocessed datasets (Sect 2.4) were eliminated in all other datasets to avoid biases due to the averaging of different periods. The resulting mean profiles (Fig. 2, left) are therefore based on an average over the 214 remaining days with at least one profile in each dataset. In addition, the absolute deviation $\Delta \boldsymbol{x}$ of the individual mean profiles from the KIMRA mean profile (Fig. 2, right) was computed using

$$\Delta \boldsymbol{x} = \boldsymbol{x}_{\text{independent}} - \boldsymbol{x}_{\text{KIMRA}} \,. \tag{3}$$

The comparison (Fig. 2) reveals that the profile shape of KIMRA deviates from the other datasets. Whereas the SD-WACCM4 and the MLS profiles are consistently more curved, the KIMRA profile shows less CO increase with altitude below 60 km and a stronger increase with altitude above 60 km. This leads to an oscillatory shape of the deviation between KIMRA and the other datasets. Furthermore, KIMRA shows a high bias above approximately 70 km that increases with altitude. The same systematic deviation was identified by Hoffmann et al. (2011) in a comparison of the KIMRA dataset to CO profiles measured by three satellite instruments including MLS. Although the reason for the deviation was not identified, it has likely to be attributed to the KIMRA measurements, since all other datasets show a consistent profile shape.

Comparing MLS and SDWACCM, the profile shapes are consistent, but SDWACCM shows slightly lower CO vmr values starting at approximtely 60 km and increasing with altitude to approximately 1 ppm at 80 km altitude. This deviation cannot be attributed to a location mismatch, since the SDWACCM AREA profile, for which the same collocation criteria as for MLS are applied, shows a similar deviation. However, the reader is reminded that, in this comparison based on KIMRA, all profiles are smoothed with the KIMRA AVK (Sect. 2.4), so that the altitude resolution at 80 km is approximately 20 km and the origin of the discrepancy is also smoothed.

ACPD
12, 559–587, 2012

4 Comparison of time series

4.1 Preparation

The CO vmr time series of the preprocessed datasets (Sect. 2.4) have been investigated altitude-wise. To do this, the complete time series, as well as the long- and short term variation alone have been considered for each altitude in the KIMRA range of sensitivity. To extract the slowly-evolving behavior of CO (here referred to as "low-frequency" variability, LF), the complete time series was Fourier transformed and the higher frequency contributions were removed by eliminating all Fourier components of periods less than 20 days. The LF part of the time series was then obtained via a reverse Fourier transformation of the modified spectrum. The short-term changes in CO (here referred to as "high-frequency" variability, HF) are calculated as the difference between the complete time series and the LF part. Note that gaps in the individual datasets were linearly interpolated before the separation to achieve an equidistant spacing of the time grid.

4.2 Visual inspection

Figure 3 shows the complete vmr time series, as well as the LF component, at 60 km. Overall, the agreement of the two measurements and the model is very good; in particular, the LF part of the time series is generally consistent during the whole period. In addition, many features of the HF behavior are similar in all datasets, e.g., the rapid drop of CO vmr at the end of January in both winters, which is caused by a SSW. During the period of strong CO variation in December 2009, KIMRA was not operational, but this variation is consistent for MLS and SDWACCM. Not all of the smaller variations are well matched among the different datasets, which is expected because of the mismatch in location and time of the individual data and the high spatial and temporal variability, which is introduced by wave activity in this atmospheric region (see also Sect. 4.4).

ACPD
12, 559–587, 2012

Not only are the variations in CO consistent among the dataset but so are the absolute CO vmr values, except for certain periods. For example, KIMRA shows three distinct periods with values lower than the other datasets, namely towards the end of 2008, during February 2010, and during April 2010. These deviations can be attributed to the KIMRA measurements, since the comparison of the mean profiles (Sect. 3), as well as Hoffmann et al. (2011), have already revealed that the KIMRA profile shape deviates systematically from other CO datasets. This leads, in particular at the 60 km level, to a negative bias for KIMRA (Fig. 2). Furthermore, it has been shown with the comparison of KIMRA and MLS profiles by Hoffmann et al. (2011) that the altitude of this maximum deviation is not constant in time. This has also been confirmed in the context of this work for the KIMRA-SDWACCM comparison (not shown). Thus, it is expected that the absolute level of the KIMRA CO vmr considered at a particular altitude level will show a time-dependent offset. It was additionally confirmed that these offsets are not obvious in the time series at altitudes where the mean profile shape deviation is small (e.g., 50 and 67 km, not shown). In February 2009 MLS shows higher values, whereas KIMRA and SDWACCM seem to be consistent. The reason for this deviation remains unclear; however, it can be stated conclusively that the simulated CO of SD-WACCM4 during the complete period is as consistent with the measurements as the measurements are with each other.

4.3 Time correlations

Correlation coefficients have been calculated at all relevant altitudes for the following pairs of time series: KIMRA-MLS, KIMRA-SDWACCM, and KIMRA-SDWACCM AREA. Again, the complete time series as well as the LF and HF parts alone have been considered. Periods in which at least one dataset of the respective pair was interpolated (Sect. 4.1) have been excluded from the computation. The resulting correlation coefficient profiles (Fig. 4) are based on approximately 270 data points (days); the respective 95 % confidence intervals are also included in Fig. 4.

The correlation KIMRA-MLS has been calculated as a guide to what can be expected from a comparison of a single-point measurement with collocated data from a spatially

ACPD
12, 559–587, 2012

distributed dataset. The LF correlation is largest, with values higher than 0.95 above 50 km. Since the complete time series is dominated by the LF variability, the correlation coefficients for the complete time series and the LF part are of similar size. Below 50 km, the correlation drops to values of about 0.7 at 40 km. Also, in the range above 50 km, the correlation coefficients vary slightly with altitude, showing maxima at approximately 53 and 73 km and a minimum at approximately 60 km. This pattern has already been seen in the deviation of the sensitivity of KIMRA from the optimal value (Sect. 2.1, Fig. 1, right). The altitudes of maximum correlation correspond to the altitudes where the sensitivity of KIMRA is closest to 1 and vice-versa, suggesting that the overall shape of the correlation profiles is governed by the KIMRA sensitivity. This causes, in particular, the relatively low values of the correlation coefficient below 50 km. The correlation of the HF part exhibits the same structure but, as expected, displays lower values of about 0.6.

The correlations of the pairs KIMRA-SDWACCM and KIMRA-SDWACCM AREA are almost identical. This suggests that the correlation analysis is not affected by sampling errors within the limits of the collocation distance and only the KIMRA-SDWACCM correlation is discussed here in detail. Although slightly lower than the KIMRA-MLS correlation coefficient, the KIMRA-SDWACCM correlation is still high, with values close to 0.9 for the complete time series, meaning that the measurement-model correlation is comparable to the measurement-measurement correlation. This is remarkable, considering that the global model is evaluated only at one grid point to be compared to the single point measurement. Furthermore, the overall shape of the KIMRA-SDWACCM correlation is also similar to that of KIMRA-MLS and thus can also be attributed to the KIMRA sensitivity characteristic and not to model behavior. However, the HF part of the KIMRA-SDWACCM correlation shows an additional feature: whereas this correlation profile is still similar to KIMRA-MLS below approximately 53 km, it decreases more rapidly with altitude to values of about 0.3 at 80 km, which is much smaller than the roughly constant value of 0.6 found for KIMRA-MLS.

ACPD
12, 559–587, 2012

The differences in the correlation coefficients for LF and HF are contrasted further in Fig. 5, which shows the profiles for $Corr_{KIMRA-MLS} - Corr_{KIMRA-SDWACCM}$ for the LF and HF cases, as well as for the complete time series. On the one hand, the difference increases with altitude above 50 km in all cases, meaning that the KIMRA-SDWACCM correlation decreases with altitude compared to the KIMRA-MLS correlation. On the other hand, this effect is much more pronounced for the HF part alone.

Note that the correlation profiles presented are generally restricted to the coarse vertical resolution of the KIMRA instrument (Sect. 2.1). To show that the main findings of this work are also valid when SD-WACCM4 is examined at higher vertical resolution, we have verified that the MLS-SDWACCM correlation exhibits a similar behavior (see supplementary material). Note, however, that the most precise direct comparison with MLS requires convolving the SD-WACCM4 dataset with the MLS averaging kernels, which was not done in the calculations presented in the supplementary material.

4.4 Interpretation

The fact that the KIMRA-SDWACCM comparison for the complete time series and the LF part is almost as good as the KIMRA-MLS comparison demonstrates that the polar winter middle atmosphere dynamics is very well represented in SD-WACCM4. Evidently, the relaxation to analyzed meteorological fields below 50 km constrains sufficiently the behavior of the simulated atmosphere, including the effect of the stratospheric winds on the parameterized gravity wave spectrum, such that the free-running part of the simulation is also close to the measurements. This, in turn, suggests that the middle atmosphere above 50 km can be regarded as a driven system, which responds to the state of the atmosphere below (cf. Liu et al., 2010).

The fact that there is still a difference in the correlation coefficients between KIMRA-SDWACCM and KIMRA-MLS, which increases with altitude, and the fact that this difference is most pronounced for the HF part, is likely due to the gravity wave parametrization in SD-WACCM4. Although SD-WACCM4 is relaxed to meteorological data, the gravity wave parameterization uses a source spectrum in the troposphere that is

ACPD
12, 559–587, 2012

realistic only in a statistical sense (Sect. 2.3). The propagation of this spectrum to the mesosphere and lower thermosphere is modulated by seasonal and intra-seasonal changes in stratospheric winds and, insofar as these winds are relaxed to observations in SD-WACCM4, the LF variability induced by gravity wave dissipation should be modeled realistically. Indeed, Fig. 4 shows that the LF correlations for KIMRA-SDWACCM are comparable to those for KIMRA-MLS. However, the detailed HF behavior of the actual spectrum of gravity waves that might be present in the atmosphere at any given time cannot be represented by the generic gravity wave spectrum included in the model. Therefore, HF variability associated with gravity waves is not captured by SD-WACCM4, even though the model is driven by observed winds, and it is expected that HF correlations with observations would be degraded accordingly. This, too, is consistent with the results shown in Fig. 4.

One might wonder whether the crossover point for relaxation to GOES-5 data provides an alternative explanation for the decreasing HF correlations between SD-WACCM4 and observations above 50 km, since the crossover occurs between 50 and 60 km. Any degradation of the wind fields in the free-running domain of the model, above the cross over point, should also impact the HF correlations. To investigate this point further, an additional model run with the same setup but with a transition to free-running between 40 and 50 km was performed and analyzed in the same way to assess the influence of the crossover point (Fig. 6). Note that the alternative crossover point was still chosen to be within the KIMRA range of sensitivity. In the new run the correlations are slightly different but the differences are insignificant with respect to the 95 % confidence interval, such that no significant impact of the cross over point on the HF correlations can be established. We conclude, therefore, that the degradation of HF correlations above 50 km is due to the fact that the gravity wave parameterization cannot represent the detailed behavior of the actual spectrum of gravity waves present in the real atmosphere, as explained above.

ACPD
12, 559–587, 2012

5 Conclusions

CO is a tracer for polar middle atmosphere dynamics; hence, a comparison of the modeled CO evolution with measurements is an indirect test of model dynamics and transport. Such a comparison is presented in this work for the Arctic winters 2008/2009 and 2009/2010 using CO measurements made with the ground-based Kiruna Microwave Radiometer (KIMRA). The instrument is located in Kiruna, Northern Sweden, and provides CO profiles between 40 and 80 km altitude. These measurements are used for a comparison to CO simulated with a recently developed version (SD-WACCM4) of the standard Whole Atmosphere Community Climate Model (WACCM). Thereby we take advantage of the ability of ground-based remote sensing to provide a consistent time series with a high temporal resolution for a particular measurement location. The comparison has therefore been performed on the smallest scales in time and space currently simulated by the model; the global model has been evaluated daily at the particular grid-point closest to Kiruna. Furthermore, this location is expected to exhibit particularly strong CO variability, since the polar vortex boundary passes occasionally over this region. The advantage of using SD-WACCM4 over free-running WACCM for this evaluation is that SD-WACCM4 is directly comparable to the measurements, since it is relaxed to analyzed meteorological data below 50 km, which also constrains the behavior at higher altitudes (Sect. 2.3). As a guide to what can generally be expected from a comparison of a single-point measurement to a spatially distributed dataset, CO measurements from the satellite instrument MLS have also been included in the analysis.

A comparison of the mean profiles, averaged over the complete period of KIMRA observations, reveals that the profile shape of KIMRA deviates similarly from both SD-WACCM4 and MLS profiles. This is consistent with a previous study, showing a similar deviation of KIMRA in comparison to data from three satellite instruments, so that this is likely a particular property of this ground-based measurement. The profile shapes of MLS and SD-WACCM4 are consistent, but SD-WACCM4 shows slightly lower values

ACPD
12, 559–587, 2012

above 60 km increasing with altitude to 1 ppm at 80 km. We have excluded the possibility that this might be caused by a mismatch in the location of the evaluated data by applying the same collocation criteria as for MLS to SD-WACCM4.

The comparison of the time evolution has been performed as a function of altitude. In addition to the evaluation of the complete time series, the low-frequency (LF) part has been separated from the rapidly varying part (HF) and both have been analyzed in the same way as the complete time series. Overall, the agreement of both measurements and the model is very good. In particular, the LF part is generally consistent during the whole period and even the HF parts shows many similarities between model and measurements. Accordingly, the measurement-model correlation coefficients of the KIMRA-SDWACCM LF time series are almost as high as the measurement-measurement (KIMRA-MLS) correlation coefficients (0.95 above 50 km). The LF correlation coefficients have only a slight altitude dependence above 50 km; below this altitude, there is a sharper decrease of the correlation (which, nonetheless, still remains as high as 0.7). This altitude dependence of the LF correlations may be attributed to the altitude dependence of the KIMRA sensitivity. The HF correlations are much smaller overall, both for KIMRA-SDWACCM and KIMRA-MLS, with a value of 0.6 around 50 km. Furthermore, above 50 km, the KIMRA-SDWACCM HF correlation decreases with increasing altitude to 0.3, whereas the KIMRA-MLS HF correlation remains approximately constant. This behavior of the measurement-model correlation has been attributed to the gravity wave parametrization in WACCM, which is based on a generic gravity wave spectrum and cannot reproduce the detailed HF behavior of the actual gravity wave spectrum that might be present at any given time in the real atmosphere.

Overall, the model is almost as consistent with the measurements as the measurements are with each other, except for the HF behavior at higher altitudes noted above. This demonstrates, that the polar winter middle atmosphere dynamics is very well represented in SD-WACCM4. This is even more remarkable considering the fact, that the global model has only been evaluated at one grid point. This shows, first, that

ACPD
12, 559–587, 2012

the relaxation to analyzed meteorological fields below 50 km constrains the behavior of the simulation sufficiently, such that the free-running part above is also close to the measurements. Second, this suggests that the upper atmosphere can be regarded as a driven system, which responds to the state at lower altitudes.

Supplementary material related to this article is available online at: http://www.atmos-chem-phys-discuss.net/12/559/2012/acpd-12-559-2012-supplement.pdf.

Acknowledgements. The analysis of the CO data was supported by the German Research Foundation (Deutsche Forschungsgemeinschaft, DFG) under projects NO 404/8-1 and PA 1714/3-2. The KIMRA instrument was initially funded by the Knut and Alice Wallenberg Foundation. Substantial support for maintenance and development of the system was provided by the Swedish National Space Board and the Kempe Foundation. A three month research visit of C. G. Hoffmann to the National Center for Atmospheric Research for the preparation of the KIMRA-WACCM comparison was funded by the German Academic Exchange Service (Deutscher Akademischer Austauschdienst, DAAD). This publication has been funded partly by Multi-TASTE. The National Center for Atmospheric Research is sponsored by the US National Science Foundation. This work is a contribution to the "Earth System Science Research School (ESSReS)", an initiative of the Helmholtz Association of German research centers (HGF) at the Alfred Wegener Institute for Polar and Marine Research. We thank the team of Aura MLS for providing the CO dataset. Finally, we would like to thank Markus Rex (Alfred Wegener Institute for Polar and Marine Research, Potsdam, Germany) and Christian von Savigny (Institute of Environmental Physics, University of Bremen) for fruitful discussions throughout the whole project.

References

Borsdorff, T. and Sussmann, R.: On seasonality of stratomesospheric CO above midlatitudes: New insight from solar FTIR spectrometry at Zugspitze and Garmisch, Geophys. Res. Lett., 36, L21804, doi:10.1029/2009GL040056, 2009. 562

ACPD
12, 559–587, 2012

Emmons, L. K., Walters, S., Hess, P. G., Lamarque, J.-F., Pfister, G. G., Fillmore, D., Granier, C., Guenther, A., Kinnison, D., Laepple, T., Orlando, J., Tie, X., Tyndall, G., Wiedinmyer, C., Baughcum, S. L., and Kloster, S.: Description and evaluation of the Model for Ozone and Related chemical Tracers, version 4 (MOZART-4), Geosci. Model Dev., 3, 43–67, doi:10.5194/gmd-3-43-2010, 2010. 566

Forkman, P., Eriksson, P., Winnberg, A., Garcia, R. R., and Kinnison, D.: Longest continuous ground-based measurements of mesospheric CO, Geophys. Res. Lett., 30, 1532, doi:10.1029/2003GL016931, 2003. 562

Fritts, D. C., Vadas, S. L., Wan, K., and Werne, J. A.: Mean and variable forcing of the middle atmosphere by gravity waves, J. Atmos. Sol.-Terr. Phy., 68, 247–265, doi:10.1016/j.jastp.2005.04.010, 2006. 561

Funke, B., Baumgaertner, A., Calisto, M., Egorova, T., Jackman, C. H., Kieser, J., Krivolutsky, A., López-Puertas, M., Marsh, D. R., Reddmann, T., Rozanov, E., Salmi, S.-M., Sinnhuber, M., Stiller, G. P., Verronen, P. T., Versick, S., von Clarmann, T., Vyushkova, T. Y., Wieters, N., and Wissing, J. M.: Composition changes after the "Halloween" solar proton event: the High Energy Particle Precipitation in the Atmosphere (HEPPA) model versus MIPAS data intercomparison study, Atmos. Chem. Phys., 11, 9089–9139, doi:10.5194/acp-11-9089-2011, 2011. 563

Garcia, R. R. and Solomon, S.: The effect of breaking gravity waves on the dynamics and chemical composition of the mesosphere and lower thermosphere, J. Geophys. Res., 90, 3850–3868, doi:10.1029/JD090iD02p03850, 1985. 568

Garcia, R. R., Marsh, D. R., Kinnison, D. E., Boville, B. A., and Sassi, F.: Simulation of secular trends in the middle atmosphere, 1950–2003, J. Geophys. Res., 112, D09301, doi:10.1029/2006JD007485, 2007. 566, 568

Hoffmann, C. G., Raffalski, U., Palm, M., Funke, B., Golchert, S. H. W., Hochschild, G., and Notholt, J.: Observation of strato-mesospheric CO above Kiruna with ground-based microwave radiometry – retrieval and satellite comparison, Atmos. Meas. Tech., 4, 2389–2408, doi:10.5194/amt-4-2389-2011, 2011. 563, 564, 565, 566, 570, 572

Kinnison, D. E., Brasseur, G. P., Walters, S., Garcia, R. R., Marsh, D. R., Sassi, F., Harvey, V. L., Randall, C. E., Emmons, L., Lamarque, J. F., Hess, P., Orlando, J. J., Tie, X. X., Randel, W., Pan, L. L., Gettelman, A., Granier, C., Diehl, T., Niemeier, U., and Simmons, A. J.: Sensitivity of chemical tracers to meteorological parameters in the MOZART-3 chemical transport model, J. Geophys. Res., 112, D20302, doi:10.1029/2006JD007879, 2007. 566

ACPD
12, 559–587, 2012

Labitzke, K. and Kunze, M.: On the remarkable Arctic winter in 2008/2009, J. Geophys. Res., 114, D00I02, doi:10.1029/2009JD012273, 2009. 561

Lamarque, J.-F., Emmons, L. K., Hess, P. G., Kinnison, D. E., Tilmes, S., Vitt, F., Heald, C. L., Holland, E. A., Lauritzen, P. H., Neu, J., Orlando, J. J., Rasch, P., and Tyndall, G.: CAM-chem: description and evaluation of interactive atmospheric chemistry in CESM, Geosci. Model Dev. Discuss., 4, 2199–2278, doi:10.5194/gmdd-4-2199-2011, 2011. 567

Lindzen, R. S.: Turbulence and stress owing to gravity wave and tidal breakdown, J. Geophys. Res., 86, 9707–9714, doi:10.1029/JC086iC10p09707, 1981. 568

Liu, H., Foster, B. T., Hagan, M. E., McInerney, J. M., Maute, A., Qian, L., Richmond, A. D., Roble, R. G., Solomon, S. C., Garcia, R. R., Kinnison, D., Marsh, D. R., Smith, A. K., Richter, J., Sassi, F., and Oberheide, J.: Thermosphere extension of the Whole Atmosphere Community Climate Model, J. Geophys. Res., 115, A12302, doi:10.1029/2010JA015586, 2010. 567

Livesey, N., Read, W., Froidevaux, L., Lambert, A., Manney, G., Pumphrey, H., Santee, M., Schwartz, M., Wang, S., Cofield, R., Cuddy, D., Fuller, R., Jarnot, R., Jiang, J., Knosp, B., Stek, P., Wagner, P., and Wu, D.: Aura Microwave Limb Sounder (MLS) — Version 3.3 Level 2 data quality and description document., Tech. rep., Jet Propulsion Laboratory, California Institute of Technology, available at: http://mls.jpl.nasa.gov/data/v3-3_data_quality_document.pdf, last access: 26 August 2011, 2011. 566

Manney, G. L., Schwartz, M. J., Krüger, K., Santee, M. L., Pawson, S., Lee, J. N., Daffer, W. H., Fuller, R. A., and Livesey, N. J.: Aura microwave limb sounder observations of dynamics and transport during the record-breaking 2009 Arctic stratospheric major warming, Geophys. Res. Lett., 36, L12815, doi:10.1029/2009GL038586, 2009. 561

Manney, G. L., Santee, M. L., Rex, M., Livesey, N. J., Pitts, M. C., Veefkind, P., Nash, E. R., Wohltmann, I., Lehmann, R., Froidevaux, L., Poole, L. R., Schoeberl, M. R., Haffner, D. P., Davies, J., Dorokhov, V., Gernandt, H., Johnson, B., Kivi, R., Kyro, E., Larsen, N., Levelt, P. F., Makshtas, A., McElroy, C. T., Nakajima, H., Parrondo, M. C., Tarasick, D. W., von der Gathen, P., Walker, K. A., and Zinoviev, N. S.: Unprecedented Arctic ozone loss in 2011, Nature, 478, 469–475, doi:10.1038/nature10556, 2011. 561

Marsh, D.: Chemical-dynamical coupling in the mesosphere and lower thermosphere, in: Aeronomy of the Earth's Atmosphere and Ionosphere, IAGA Special Sopron Book Series, vol. 2, 1st edn., Springer, Dordrecht, 3–17, 2011. 563

ACPD
12, 559–587, 2012

Minschwaner, K., Manney, G. L., Livesey, N. J., Pumphrey, H. C., Pickett, H. M., Froidevaux, L., Lambert, A., Schwartz, M. J., Bernath, P. F., Walker, K. A., and Boone, C. D.: The photochemistry of carbon monoxide in the stratosphere and mesosphere evaluated from observations by the microwave limb sounder on the aura satellite, J. Geophys. Res., 115, D13303, doi:10.1029/2009JD012654, 2010. 562

Pumphrey, H. C., Filipiak, M. J., Livesey, N. J., Schwartz, M. J., Boone, C., Walker, K. A., Bernath, P., Ricaud, P., Barret, B., Clerbaux, C., Jarnot, R. F., Manney, G. L., and Waters, J. W.: Validation of middle-atmosphere carbon monoxide retrievals from the microwave limb sounder on aura, J. Geophys. Res.-Atmos., 112, D24S38, doi:10.1029/2007JD008723, 2007. 566

Richter, J. H., Sassi, F., and Garcia, R. R.: Toward a Physically Based Gravity Wave Source Parameterization in a General Circulation Model, J. Atmos. Sci., 67, 136–156, doi:10.1175/2009JAS3112.1, 2010. 566

Rodgers, C. D.: Inverse Methods for Atmospheric Sounding, World Scientific Publishing, London, 2000. 564

Shepherd, T. G.: Transport in the Middle Atmosphere, J. Meteorol. Soc. Jpn. B, 85, 165–191, 2007. 561

Solomon, S., Garcia, R. R., Olivero, J. J., Bevilacqua, R. M., Schwartz, P. R., Clancy, R. T., and Muhleman, D. O.: Photochemistry and transport of carbon monoxide in the middle atmosphere, J. Atmos. Sci., 42, 1072–1083, 1985. 562

Waters, J., Froidevaux, L., Harwood, R., Jarnot, R., Pickett, H., Read, W., Siegel, P., Cofield, R., Filipiak, M., Flower, D., Holden, J., Lau, G., Livesey, N., Manney, G., Pumphrey, H., Santee, M., Wu, D., Cuddy, D., Lay, R., Loo, M., Perun, V., Schwartz, M., Stek, P., Thurstans, R., Boyles, M., Chandra, K., Chavez, M., Chen, G., Chudasama, B., Dodge, R., Fuller, R., Girard, M., Jiang, J., Jiang, Y., Knosp, B., LaBelle, R., Lam, J., Lee, K., Miller, D., Oswald, J., Patel, N., Pukala, D., Quintero, O., Scaff, D., Snyder, W. V., Tope, M., Wagner, P., and Walch, M.: The Earth observing system microwave limb sounder (EOS MLS) on the aura Satellite, IEEE T. Geosci. Remote Sens., 44, 1075–1092, doi:10.1109/TGRS.2006.873771, 2006. 565

ACPD
12, 559–587, 2012

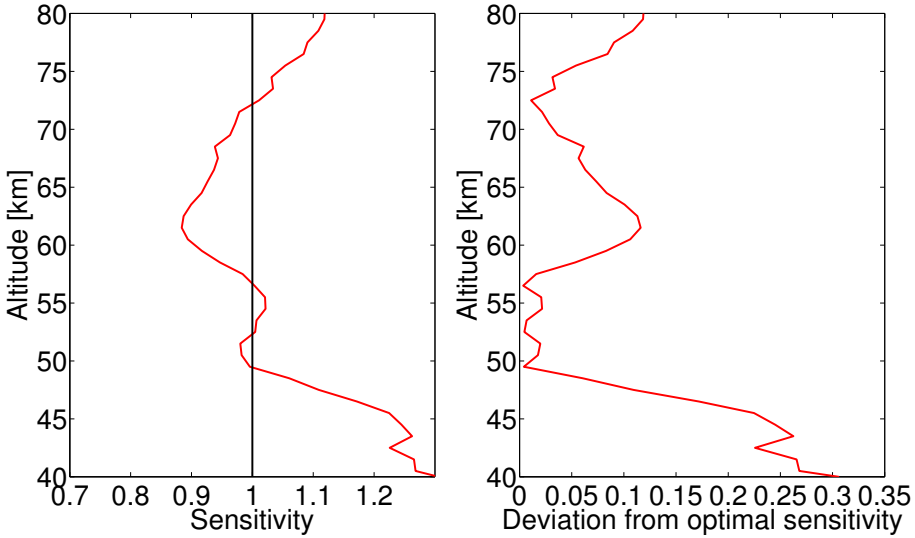

Fig. 1. Left: Sensitivity of the KIMRA measurements as given by the sum of the AVK functions. Right: Absolute deviation of the sensitivity from unity. See text for details.

ACPD
12, 559–587, 2012

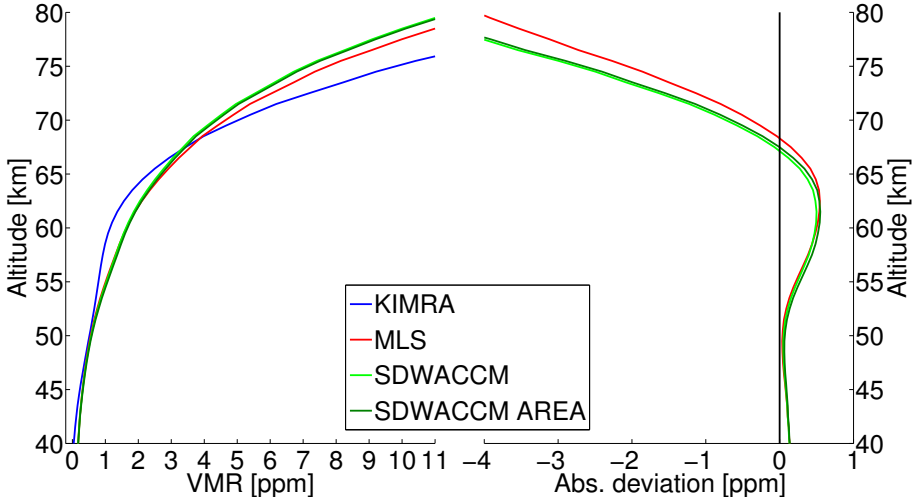

Fig. 2. Comparison of mean profiles for the different datasets. Left: Mean profiles. Right: Deviation between the KIMRA and the SDWACCM profiles calculated with Eq. (3).

ACPD
12, 559–587, 2012

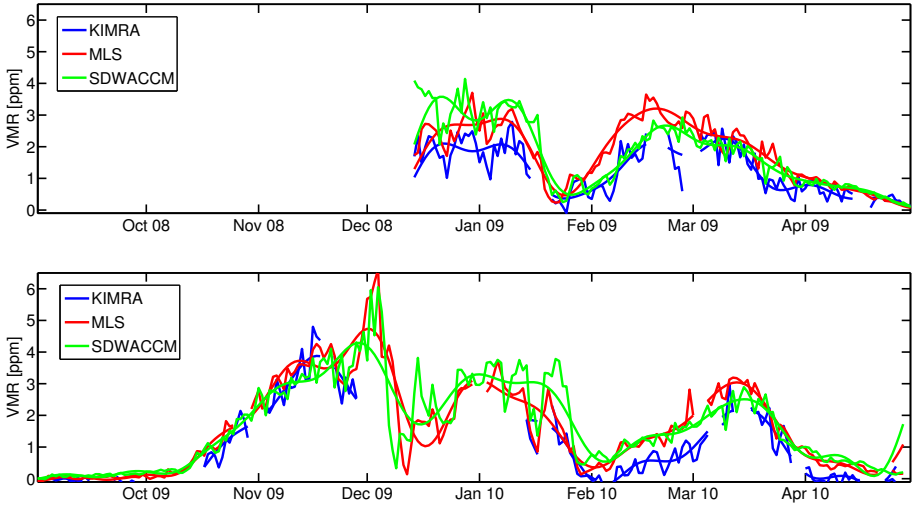

Fig. 3. Evolution of the CO vmr at 60 km, as measured by KIMRA and MLS and as simulated by SD-WACCM during the full KIMRA period. The smooth curves are the LF variations, obtained by eliminating all Fourier components with periods less than 20 days from the spectrum of the time series. See text for details.

ACPD
12, 559–587, 2012

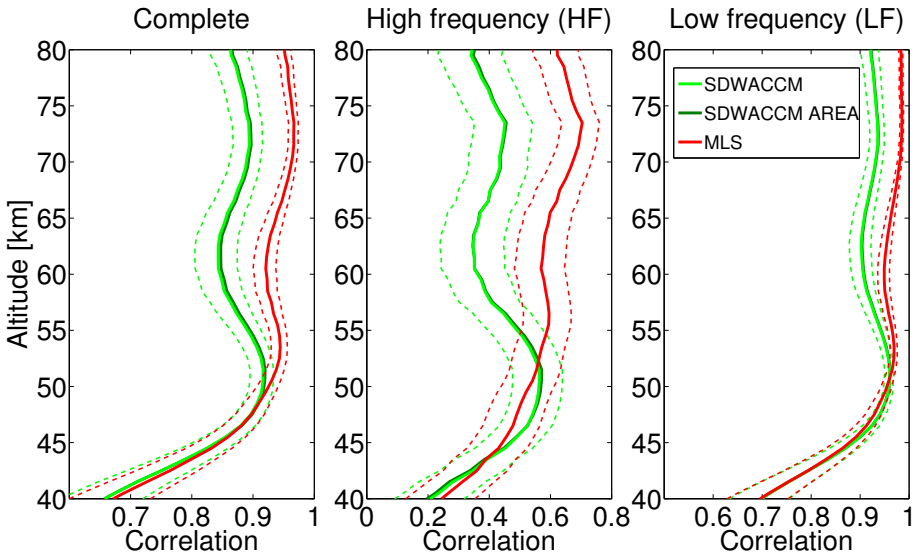

Fig. 4. Altitude profiles of the correlation coefficients of the KIMRA-SDWACCM, KIMRA-SDWACCM AREA, and KIMRA-MLS data for the complete time series (left panel), for the high frequency part alone (middle panel), and for the low frequency part alone (right panel). The dashed lines indicate the 95 % confidence interval of the correlation coefficients. The KIMRA-SDWACCM AREA correlations can hardly be seen, as they are almost identical with the KIMRA-SDWACCM correlations.

ACPD
12, 559–587, 2012

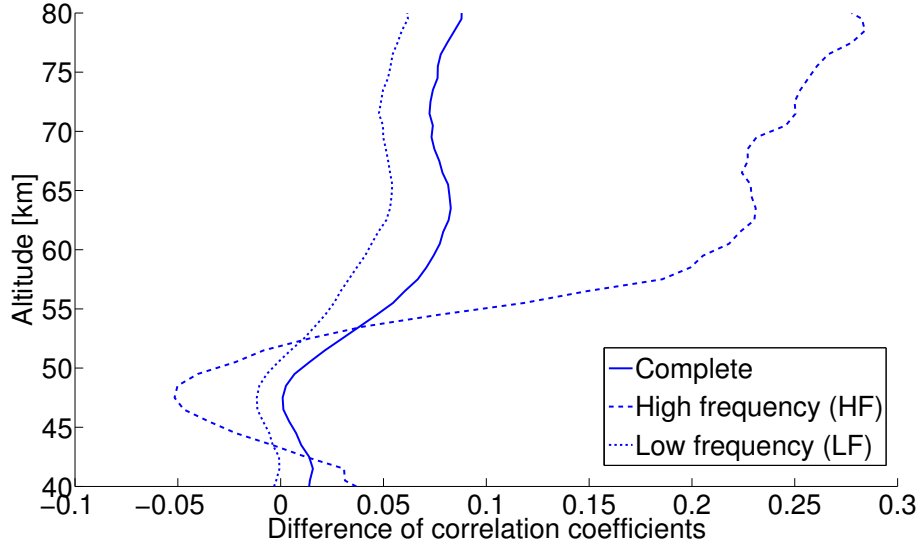

Fig. 5. Differences between the correlation coefficients of KIMRA-MLS and KIMRA-SDWACCM for the complete time series as well as for the high frequency and low frequency parts. The correlation coefficients alone are shown in Fig. 4.

ACPD
12, 559–587, 2012

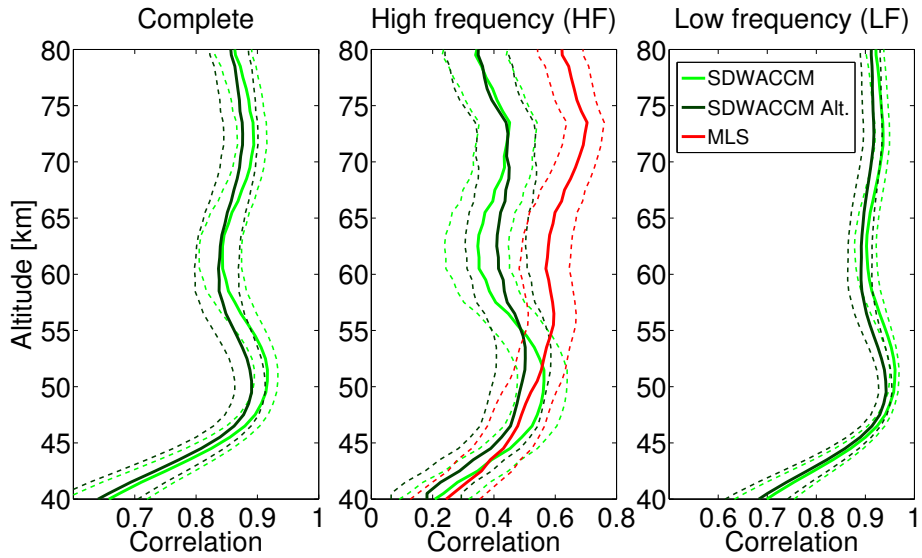

Fig. 6. Altitude profiles of the correlation coefficients as in Fig. 4, but for the alternative KIMRA-SDWACCM comparison, which is based on a crossover point that is lower (between 40 and 50 km) than for all other SD-WACCM data shown in this paper. The original correlations for KIMRA-SDWACCM (as well as KIMRA-MLS for the high frequency part) are shown here only for comparison and are the same as in Fig. 4. The dashed lines indicate the 95 % confidence interval of the correlation coefficients.

ACPD
12, 559–587, 2012